Journal of Power Sources 240 (2013) 721–728

Contents lists available at SciVerse ScienceDirect

Journal of Power Sources

journal homepage: www.elsevier.com/locate/jpowsour

Electrochemical characterization of Ni–yttria stabilized zirconia electrode for hydrogen production in solid oxide electrolysis cells

Hari Prasad Dasari [a], Sun-Young Park [a], Jeonghee Kim [a,b], Jong-Ho Lee [a], Byung-Kook Kim [a], Hae-June Je [a], Hae-Weon Lee [a], Kyung Joong Yoon [a,*]

[a] High-Temperature Energy Materials Research Center, Korea Institute of Science and Technology, Seoul, South Korea
[b] Department of Fuel Cells and Hydrogen Technology, Hanyang University, Seoul, South Korea

HIGHLIGHTS

- The electrochemical behavior of Ni–YSZ electrode is studied for steam electrolysis.
- The high-frequency impedance is due to charge transfer across the Ni/YSZ interface.
- The mid-frequency impedance is due to gas–solid interaction.
- Polarization resistance decreases with increasing the reactant concentration.
- The minimum impedance is observed at H_2–50% H_2O in electrolysis mode.

ARTICLE INFO

Article history:
Received 18 February 2013
Received in revised form
30 April 2013
Accepted 11 May 2013
Available online 18 May 2013

Keywords:
Solid oxide electrolysis cell
Solid oxide fuel cell
Impedance spectroscopy
Rate limiting process

ABSTRACT

Electrochemical performance of Ni–yttria stabilized zirconia (YSZ) electrode, which is widely used as the anode for solid oxide fuel cells (SOFCs), is evaluated for H_2 production in solid oxide electrolysis cells (SOECs). The impedance spectra of Ni–YSZ electrode are composed of two major depressed arcs. The high-frequency impedance ($>10^4$ Hz) can be assigned to transfer of the charged species across the Ni/YSZ interface, and the mid-frequency arc ($10^2 \sim 10^3$ Hz) is possibly associated with the gas–solid interaction such as adsorption, dissociation, desorption, etc. The impedance spectra are strongly influenced by the gas composition in both fuel cell (H_2 oxidation) and electrolysis (H_2O reduction) reactions; polarization resistance decreases with increasing concentration of the reactant species. In fuel cell mode, both high- and mid-frequency arcs increase with decreasing H_2 concentration, while the impedance spectra are dominated by the mid-frequency arc and the high-frequency arc remains negligible even at low H_2O concentration in electrolysis mode. Reaction mechanisms and elementary reaction pathways for H_2 oxidation and H_2O reduction are suggested based on impedance spectra. The minimum impedance is observed at 50% H_2O in electrolysis mode, and further increase in H_2O concentration causes degradation of the electrode performance, possibly due to local oxidation of Ni.

1. Introduction

Hydrogen is one of the leading candidates as storable, transportable, and environmentally benign fuel and energy carrier for a future energy supply system. Although hydrogen is abundant in nature, it is found as compounds combined with other elements, and thus, hydrogen production always requires energy inputs. Currently, fossil fuel is used for most of the hydrogen production processes including steam reforming of methane, partial oxidation of heavy hydrocarbons, and gasification of coal. These methods are not viable in a long-term perspective due to consumption of non-renewable sources and emission of green house gases. Therefore, there is a high level of interest in developing clean and efficient technique for large-scale and high-purity hydrogen production. High temperature solid oxide electrolysis cell (SOEC) technology is one of the promising alternatives when combined with the renewable energy sources such as wind power, solar energy, hydropower and geothermal power [1–7]. Basically, SOEC converts water into gaseous hydrogen and oxygen using DC electricity and heat, and the overall reaction of the water electrolysis is the reverse

* Corresponding author. Korea Institute of Science and Technology, High-Temperature Energy Materials Research Center, Hwarangno 14-gil 5, Seongbuk-gu, Seoul 136-791, Korea. Tel.: +82 2 958 5515; fax: +82 2 958 5529.
E-mail addresses: kjyoon@kist.re.kr, kyungjoong.yoon@gmail.com (K.J. Yoon).

0378-7753/$ – see front matter © 2013 Elsevier B.V. All rights reserved.
http://dx.doi.org/10.1016/j.jpowsour.2013.05.033

of solid oxide fuel cell (SOFC) reaction. Thus, in principle, the identical cell can operate as both SOFC and SOEC [8], and SOEC research can directly benefit from the knowledge and experience accumulated in the SOFC technology. However, two operating modes differ in the electric potential gradient and gas environments, which can significantly affect performance and long-term stability of the cell. Thus, in recent years, increasing efforts have been made to understand the phenomena which specifically occur under the operating conditions of SOECs [9–16].

One of the distinct features of SOEC operation is high steam concentration at the hydrogen electrode. The state-of-the-art hydrogen electrode for SOECs is a cermet of Ni and yttria-stabilized zirconia (YSZ), which is the most commonly used anode material for SOFCs. Under high steam conditions in SOEC operation, performance of Ni–YSZ electrode may be influenced by agglomeration and/or evaporation of Ni [17–19], and segregation of impurities to the triple phase boundaries (TPBs) [20,21]. Presence of steam leads to formation of nickel hydroxide complexes (Ni_2-OH) and accelerates surface transport, resulting in severe agglomeration of Ni and reduction of TPBs, as shown by experiments [17,18] as well as DFT calculations [19]. Local depletion as well as enrichment of Ni is also expected with presence of water vapor via evaporation in the form of $Ni(OH)_2$ since the partial pressure of $NiOH_2$ (g) is proportional to the activity of O_2 (g) and approximately six orders of magnitude higher than that of Ni (g) in typical SOEC operating conditions [17]. In addition, glass sealant could be the main source of the Si-containing impurities originating from corrosive attack by water vapor at high temperatures [15]. Gaseous $Si(OH)_4$ leads to the electrode poisoning through formation of glassy phase silicates at TPBs upon the current load for steam reduction [20,21]. Based on these technical challenges confronted in SOEC operation with excess amount of steam, the standard Ni–YSZ electrode for SOFCs may not be appropriate, and development of novel electrode materials and microstructure specialized for SOECs would be required to obtain high performance and long-term stability. For such purposes, it is very important to understand the reaction mechanisms and kinetics of the Ni–YSZ electrode because detailed knowledge on various aspects of the electrode reactions allows identification of current limitations and determination of future research direction. In this study, the impedance spectra of the Ni–YSZ symmetric half cell were obtained under various operating conditions, and physical origins of the impedance arcs at various frequency ranges were identified for both SOEC and SOFC mode operations. Based on comprehensive understanding of the electrode reaction kinetics, rate limiting processes for SOEC and SOFC were suggested, and optimum condition for SOEC operation was proposed.

2. Experimental

Symmetrical Ni–YSZ/YSZ/Ni–YSZ half cells were constructed using 2.9 mm-thick YSZ discs (Nikkato Corp. Japan) as electrolyte substrates. NiO/YSZ cermet paste was prepared by mixing precursor powders with desired amounts of solvent (α-terpineol, Kanto chemicals, Japan), binder (Ethyl cellulose (EC), Aldrich Chemicals, USA), dispersant (Hypermer (KD-1), Uniqema, United Kingdom), and plasticizer (Dibutyl phthalate (DBP), Junsei chemicals, Japan). The working and counter electrodes were formed by screen-printing the paste on the two sides of the YSZ disc, followed by sintering at 1370 °C for 3 h. A reference electrode with ring geometry was employed by positioning an Au wire in the mid-way between the working and counter electrodes around the outer rim of the electrolyte pellet. The Au wire was placed in a groove carved into the electrolyte pellet to prevent the wire from moving away from the original position and ensure that the reference electrode remains in the region of defined potential. The Au mesh was used as current collectors at the working and counter electrodes.

The half cell was placed at the center of the quartz tube reactor inside a tube furnace. The reactor was heated in an electric furnace equipped with a K-type thermocouple placed adjacent to the cell. The electrodes were reduced in humidified hydrogen (3% H_2O) at 750 °C for 4 h before the electrochemical measurements. A cold trap was placed at the outlet of the reactor to condense the water from the effluent gas stream to ensure that there is no back pressure in the reactor. Electrochemical measurements were performed using Solartron 1260/1287 frequency response analyzer and potentiostat using the AC signal strength of 10 mV to acquire the impedance data. The electrochemical impedance spectra were collected under various operating temperatures (700–850 °C), H_2/H_2O ratios, and DC bias (positive bias, negative bias and at OCV), and the obtained data were analyzed by fitting into equivalent circuit model using Z-view 3.1C software. The current densities at ±0.2 V and ±0.1 V were in the range of 20–30 mA cm^{-2} and 10–15 mA cm^{-2}.

3. Results and discussion

There are five typical geometries of the reference electrode reported in the literature; circular planer [22–24], square planer [25,26], riso-geometry [27,28], ring-type [29,30] and inter-digitated type. The circular planer, square planer, inter-digitated types of geometries generally suffer from a lack of a separate environment for the reference electrode, and is therefore often unsuited for use when the working electrode is subjected to changing partial pressures. For riso-type geometry the disadvantage is the complexity of fabrication with unusual geometry which makes it difficult to use with standard experimental rigs, although this has been done. The hole bored through the electrolyte can disrupt the potential distribution and the thick electrolyte will contribute a significant ohmic resistance, which must be corrected for. In ring-type geometry, a thick electrolyte with working and counter electrodes was deposited on opposite sides. The reference electrode is a thin platinum/gold wire positioned mid-way between the active electrodes around the outer rim of the electrolyte, which may be in the separate environment. However, the thick electrolyte and large distance between working and reference electrodes required to ensure errors in the wire placement are minimized, will introduce significant ohmic losses that must be corrected. Winkler et al. [26] suggested placing the wire in a groove carved into the electrolyte, to prevent the wire from moving from a fixed lateral position, and ensure that the reference electrode remains in a region of defined potential. In the present study ring-type geometry has been employed and to enhance the gold-wire/YSZ–electrolyte contact, the carved groove on the electrolyte and the gold wire were further brushed with gold paste.

Fig. 1(a) and (b) shows the Nyquist and Bode plots of the EIS data, respectively, obtained from the symmetrical half cell (Ni–YSZ/YSZ/Ni–YSZ) at 700–850 °C in H_2–3% H_2O environment under open circuit conditions. In Nyquist plot (Fig. 1(a)), the high frequency intercept on the real axis corresponds to the Ohmic resistance of the cell including the contribution of the YSZ electrolyte [31], and was normalized to the value of zero. The total polarization resistance of the electrode, which is obtained by subtracting high frequency intercept from low frequency intercept [31], was 0.48 Ω cm^2 at 850 °C, 0.87 Ω cm^2 at 800 °C, 1.63 Ω cm^2 at 750 °C, and 2.77 Ω cm^2 at 700 °C, indicating that the electrode polarization is dominated by thermally activated processes. It is widely accepted that the impedance spectra of the Ni–YSZ cermet electrode operating in H_2–H_2O atmosphere are composed of several overlapping semicircles, implying that the H_2–H_2O electrode reaction consists

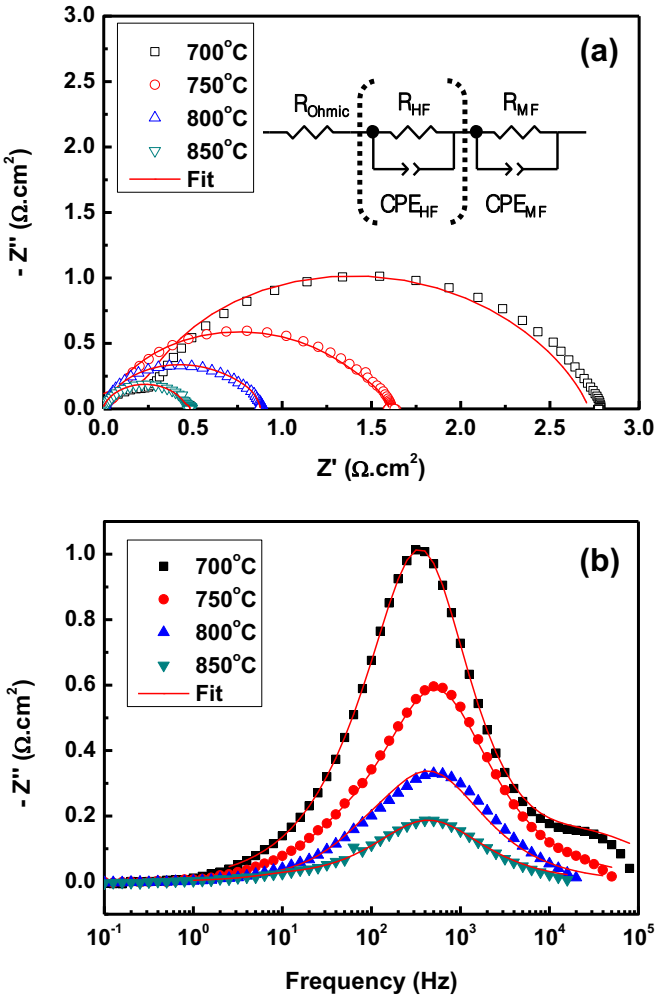

Fig. 1. (a) Nyquist and (b) Bode plots of the EIS data obtained from the symmetrical half cell (Ni–YSZ/YSZ/Ni–YSZ) at 700–850 °C in H_2–3% H_2O environment under open circuit conditions. Equivalent circuit used for fitting is shown in (a).

of at least two rate-limiting processes [32–34]. It has been suggested that the rate-limiting process could be adsorption/dissociation of the reactant species [34–36], surface migration [36], charge transfer reaction [35,37], desorption of product species [38], and gas diffusion [39]. Although numerous studies have been reported by far [33,35,40–46], the elementary mechanism of the H_2–H_2O reaction on the Ni–YSZ electrode is still controversial and has not been conclusively determined yet. The impedance spectra are strongly influenced by the preparation method and resulting structure of the electrode [33,47], and complex microstructure of the Ni–YSZ cermet electrode imposes difficulties in interpreting the experimental data and achieving the fundamental understanding. Therefore, it is necessary to understand the reaction mechanism and rate-limiting processes of the Ni–YSZ electrode used in this study prior to investigation on the electrochemical behavior under electrolysis operation. In the impedance spectra in Fig. 1(a) and (b), the high-frequency (>10^4 Hz) and mid-frequency (10^2–10^3 Hz) arcs are readily recognized at 700–800 °C. At 850 °C, the mid-frequency impedance becomes dominant and the contribution of the high-frequency arc appears to be negligible. The equivalent circuit models can be effectively used for interpretation of the impedance spectra and identification of the physical origin of the impedance features. In this work, the obtained spectra were fitted into the equivalent circuit model consisting of one or two standard resistor (*R*)-constant phase element (*CPE*) units as illustrated in the insert of Fig. 1(a). The *CPE* in the equivalent circuit is used to analyze the frequency dispersion observed in the solid electrode/electrolyte systems [48], and the empirical equation for the impedance of *CPE* is expressed as:

$$Z_{\mathrm{CPE}} = C(j\omega)^{-n} \quad (1)$$

where C is a pseudo-capacitance, $j = \sqrt{-1}$, ω is the angular frequency, and n is the exponent component. The number of *R-CPE* units used for fitting was determined by the number of rate-limiting processes, i.e. one unit for 850 °C and two units for 700–800 °C. Fitting results represented by the solid lines in Fig. 1(a) and (b) confirm good fits, and the obtained resistance and capacitance values are summarized in Table 1.

In order to identify the physical origins of the two impedance arcs, temperature dependence of the high-frequency and mid-frequency resistances, R_{HF} and R_{MF}, respectively, was illustrated in Fig. 2. The R_{HF} was strongly dependent on temperature with the activation energy of 2.1 eV. The high frequency impedance with the characteristic frequency larger than 10^4 Hz is commonly assigned to the electrode electrochemistry arising from the charge transfer reaction or electrical double layer at the two phase boundaries [33,45]. The strong temperature-dependence observed from R_{HF} is a typical behavior of charge transfer reaction [33]. The high-frequency capacitance (C_{HF}) obtained from the equivalent circuit fitting is in the range of 22–46 μF cm^{-2}. The capacitance of the double layer for charge transfer reaction at the metal–solid electrolyte interface can be estimated using the Gouy–Chapman theory with Stern's modification [49,50], and the capacitance of the compact double layer at the Ni/YSZ interface is calculated to be ~30 μF cm^{-2} [33]. In addition, the double layer capacitances of the Pt/YSZ and Au/YSZ interfaces were reported to be 0.5–1.4 μF cm^{-2} and 20–40 μF cm^{-2}, respectively [49,51]. Considering the rough and inhomogeneous structure of the practical Ni/YSZ cermet electrode used in this study, the high-frequency capacitance values (C_{HF}) obtained from fitting (Table 1.) are in reasonably good agreement with the reported values for metal/YSZ double layers including Ni/YSZ interface [33,49,51]. Based on the analysis of the resistance and capacitance, the rate limiting process for high-frequency impedance is considered to be transfer of the charged species across the Ni/YSZ interface. This conclusion is also supported by the previous report which assigned the high frequency feature of the Ni–YSZ electrode to the relaxation process of the electrical double layer coupled with the charge transfer process of the electrochemical reaction [44].

The mid-frequency arc showed the activation energy of ~0.8 eV in Fig. 2, and the capacitance was found to be 313 μF cm^{-2} at 850 °C, 687 μF cm^{-2} at 800 °C, 1112 μF cm^{-2} at 750 °C, and 1643 μF cm^{-2} at 700 °C from the equivalent circuit fitting. Given the available information of the activation energy and capacitance values for elementary reaction steps [33,45,46,52], the reasonable explanation for the mid-frequency process could be the gas–solid interaction (adsorption, dissociation, desorption, etc.) or surface diffusion of the adsorbed species. Strong temperature dependence

Table 1
Polarization resistance and capacitance at 700–850 °C in H_2–3% H_2O under open circuit conditions obtained from equivalent circuit fitting.

Temperature (°C)	R_{HF} (Ω cm^2)	R_{MF} (Ω cm^2)	C_{HF} (μF cm^{-2})	C_{MF} (μF cm^{-2})
850	–	0.48	–	313
800	0.05	0.82	22	687
750	0.14	1.49	31	1112
700	0.55	2.22	46	1643

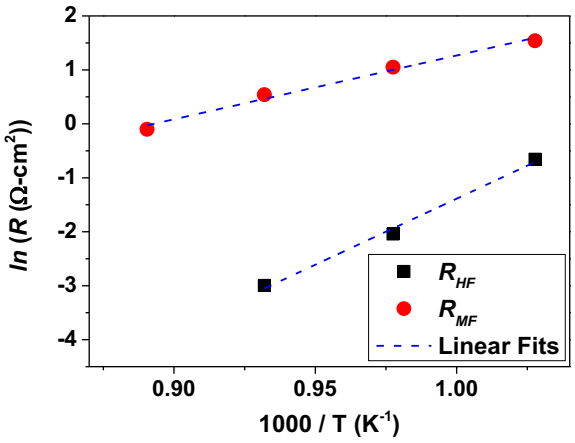

Fig. 2. Temperature dependence of R_{HF} and R_{MF} at 700–850 °C.

of the capacitance suggests that the capacitance could be associated with the concentration change of adsorbed species close to the TPBs since surface concentration strongly depends on temperature [53]. The H_2O dependence of the mid-frequency impedance in Fig. 3 further supports the physical origin of the arc. It is known that dissociative adsorption and diffusion processes of hydrogen on Ni are remarkably enhanced by increasing H_2O content up to certain level [34,40,45,54]. Presence of oxygen species on the electrode surface resulting from H_2O–Ni interaction greatly accelerates dissociative adsorption and diffusion processes of hydrogen although the site density on the Ni surface available for hydrogen adsorption is reduced by competitive adsorption of oxygen [55–57]. Fig. 3 shows significant reduction of the mid-frequency arc with increasing H_2O content, which supports the argument that the mid-frequency arc could be related to the gas–solid interaction or surface diffusion of the adsorbed species.

A shift in the imaginary components toward lower frequency or higher frequency can be noticed with the changes in the H_2–H_2O–N_2 fuel mixtures [44], surface chemistry and varying H_2O content [58]. From the measured and predicted reaction-diffusion impedance for H_2–H_2O–N_2 fuel mixtures without detailed surface chemistry, it has been reported that with the decrease of H_2O content the frequency at the peak of the arc of the imaginary component has been decreased. With detailed surface chemistry and at a fixed specific surface area, under open circuit conditions, it has been predicted that the imaginary component has been increased with the increase of H_2O content [58]. This effect is attributed to the relative surface-coverage variations with the H_2O concentration. The surface adsorbed H_2O significantly decreases as the gas-phase H_2O concentration decreases. Therefore, the surface adsorbates, which are the result of surface kinetics and gas-phase compositions, represent the ability of the surface to store the associated gas-phase species. The H_2O on the surface is relatively low when gas-phase H_2O concentration is low, resulting in a lower storage capacity for H_2O and a relatively small frequency shift. Bessler et al., [40] has established a tentative thermodynamic model in order to investigate the influence of equilibrium-potential effects on the hydrogen oxygen kinetics at SOFC Ni/YSZ anodes. Three different reaction pathways (oxygen spillover, hydrogen spillover, interstitial hydrogen spillover), based on five different elementary charge-transfer reactions, were studied and concluded that all charge-transfer reactions show a strong and highly non-linear dependence of their kinetic on gas phase H_2 and H_2O concentration due to equilibrium-potential effects. Similar to Zhu et al. [58] observations, in our studies, for the imaginary component (Fig. 3), a shift toward high frequency is noticed with the decrease in the H_2O content and this indicates that the surface chemistry plays a key role with the variation in the H_2O content.

Since the origins of the high- and mid-frequency impedance arcs were identified, electrochemical behavior of the Ni–YSZ electrode in fuel cell and electrolysis operation was examined. Fig. 4

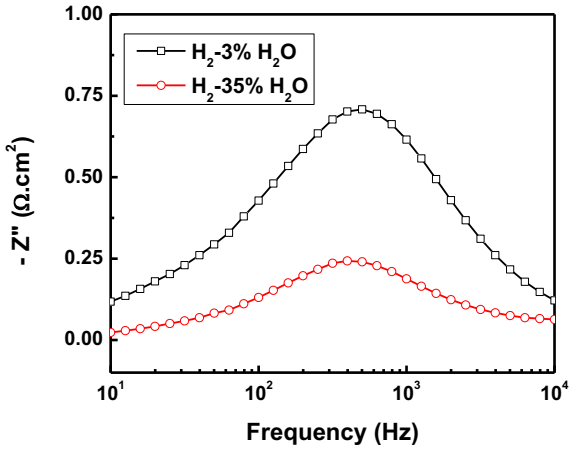

Fig. 3. Bode plot of the imaginary part of the impedance spectra measured at 750 °C in H_2–3% H_2O and H_2–35% H_2O under open circuit condition.

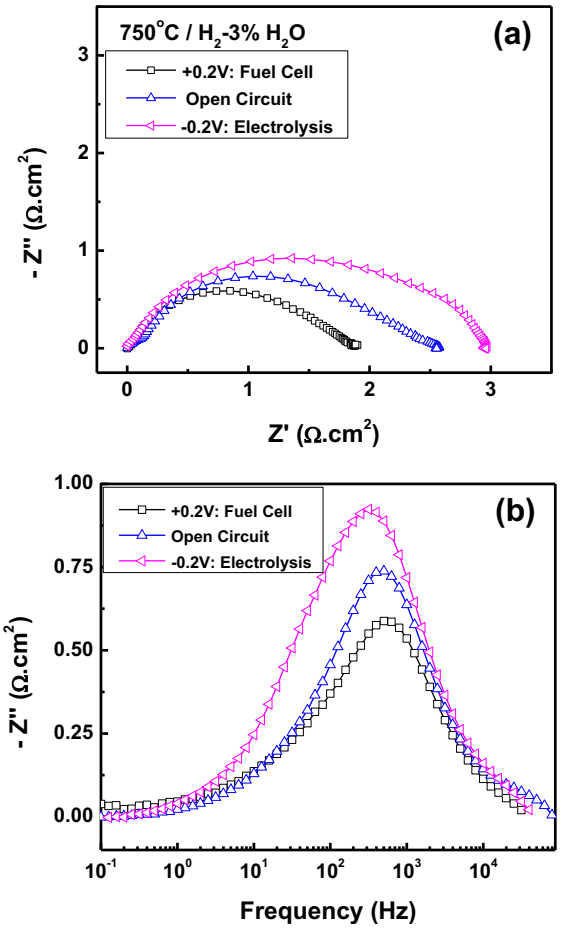

Fig. 4. (a) Nyquist and (b) Bode plots of the impedance spectra measured at 750 °C in H_2–3% H_2O under various polarization (+0.2 V, 0 V, and −0.2 V).

shows the impedance spectra measured at 750 °C in H_2–3% H_2O under the various electrode potentials. The positive bias applied to the Ni–YSZ electrode leads to H_2 oxidation reaction which represents the anode process of fuel cell. This reaction is believed to occur near the TPBs, and can be formulated as;

$$H_2(gas) + O^{2-}(YSZ) \rightarrow H_2O(g) + 2e^-(Ni) \quad (2)$$

The negative bias drives dissociation of H_2O into H_2 gas and oxygen ion, which corresponds to the cathode reaction in the electrolysis process. This reaction can be expressed as the reverse process of eq. (2);

$$H_2O(gas) + 2e^-(Ni) \rightarrow H_2(g) + O^{2-}(YSZ) \quad (3)$$

In Fig. 4(a), the overall polarization resistance was reduced in fuel cell mode and increased in electrolysis mode, which can qualitatively be explained by the concentration of reactant species for each reactant. The H_2 concentration was sufficiently high to sustain the fuel cell reaction while deficiency of H_2O caused large impedance for electrolysis reaction. The Bode plot of the imaginary part in Fig. 4(b) shows that the major variation in the impedance with the applied bias occurred at the mid-frequency arc, which is consistent with our previous statement that the mid-frequency arc strongly depends on the concentration of the reactant species. The high-frequency arc was relatively insensitive to the applied bias in this condition.

When the H_2O content was increased to 50%, completely different behavior was observed in Fig. 5. The trend of the total polarization resistance was the opposite; it was larger in fuel cell reaction and smaller in electrolysis reaction (Fig. 5(a)). Bode plot in Fig. 5(b) reveals the response of the individual impedance arcs to the applied potential as a function of frequency. The high-frequency arc increased with positive bias (fuel cell reaction) and virtually disappeared with negative bias (electrolysis reaction). The mid-frequency arc slightly increased in fuel cell reaction and decreased in electrolysis reaction, which is opposite from Fig. 4(b). In addition, the low-frequency arc at frequency range of 1–10 Hz was noticed only in fuel cell reaction. The impedance data in Figs. 4 and 5 indicate that the kinetics for H_2 oxidation and H_2O dissociation are strongly influenced by the gas composition. Since the global reactions for H_2 oxidation and H_2O dissociation consist of multiple elementary steps, it is necessary to understand how the reaction pathways and rate limiting processes are affected by the gas composition in order to interpret the electrochemical behavior in Figs. 4 and 5. The first step of H_2 oxidation process in fuel cell reaction is the interaction between H_2 gas molecules and the electrode surface. Hydrogen exhibits various chemisorptive and physisorptive behaviors on the solid depending on the physical, chemical, and electronic nature of the surface [59]. For Ni–YSZ electrode, adsorption of hydrogen occurs favorably on the surface of Ni which has a high density of d-electron states [36,59]. Since there is no energy barrier for the dissociation of hydrogen on a Ni surface at high temperatures [36], nearly all hydrogen molecules hitting the Ni surface dissociate and adsorb in the atomic form. For oxidation reaction, atomic hydrogen adsorbed on the Ni surface can move over the Ni–YSZ interface toward the YSZ, and simultaneously transfer the electrons to the Ni electrode, attaching to either O^{2-} or OH^- on the YSZ surface. In this pathway, hydrogen adsorbs on the Ni surface and water desorbs from the YSZ surface. It is referred to as "hydrogen spillover". Alternatively, oxygen ions on the YSZ surface can move over the Ni–YSZ interface toward the Ni surface and transfer electrons to Ni, which is called "oxygen spillover". In this case, hydrogen adsorbs on the Ni surface, and water also desorbs from the Ni surface. For clarification of terminology,

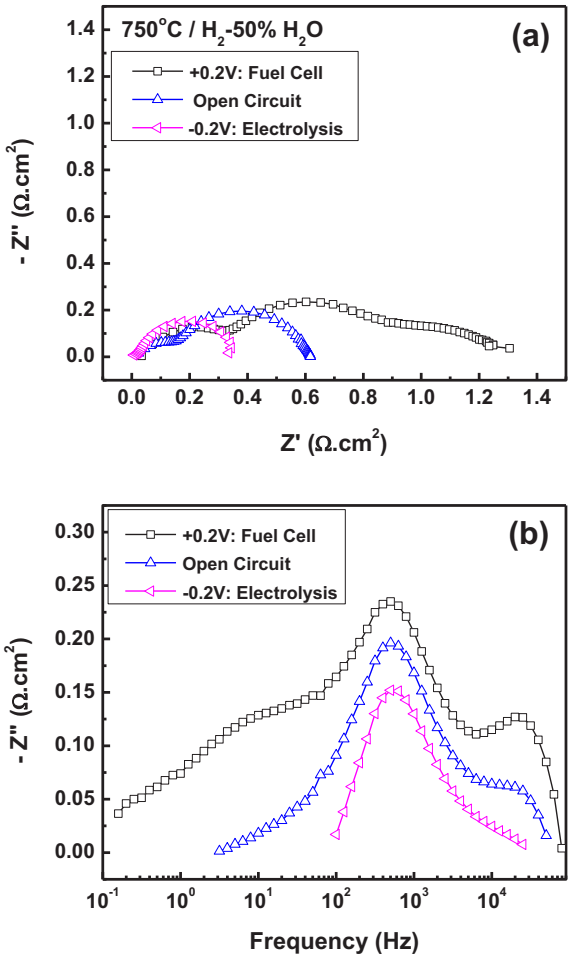

Fig. 5. (a) Nyquist and (b) Bode plots of the impedance spectra measured at 750 °C in H_2–50% H_2O under various polarization (+0.2 V, 0 V, and −0.2 V).

"spillover" refers to transition of surface species across the boundary between two different materials. The surface diffusivity of atomic hydrogen on Ni surface (9.2×10^{-4}–1.2×10^{-3} $cm^2\ s^{-1}$ at 973 K [41,60,61]) is significantly higher than that of oxygen ion on YSZ (8.1×10^{-12}–7.3×10^{-11} $cm^2\ s^{-1}$ at 973 K [62–64]). Such difference in surface diffusivities can be explained by the small size of the hydrogen atom and the small number of formal bonds made with the surface [34,45]. Fast transport of adsorbed hydrogen on the Ni surface suggests that the hydrogen spillover mechanism would be dominant over the oxygen spillover mechanism. Furthermore, decrease of charge transfer resistance with increasing H_2 partial pressure observed in Figs. 4 and 5 supports the hydrogen spillover mechanism because the resistance should increase with increasing H_2 partial pressure for oxygen spillover mechanism according to the elementary kinetic modeling results [34]. It was also demonstrated by both theoretical [42] and experimental [34] approaches that hydrogen spillover is a dominant pathway for charge transfer reactions in H_2 oxidation process on Ni/YSZ electrode, whereas oxygen spillover is valid for Pt/YSZ electrodes as shown by photoelectron emission microscopy [65] and cyclovoltammetry [66]. For hydrogen spillover, the charge transfer reaction could occur via following pathways;

$$H(Ni) + O^{2-}(YSZ) \rightarrow OH^-(YSZ) + e^-(Ni) \quad (4)$$

$$H(Ni) + OH^-(YSZ) \rightarrow H_2O(YSZ) + e^-(Ni) \quad (5)$$

The first step for H_2O dissociation is the interaction between H_2O gas molecules and Ni–YSZ electrode. It was reported that interaction of H_2O with Ni leads to a nearly complete dissociation of H_2O molecules, and adsorbed water molecule, hydroxide, and hydroxyl species virtually do not exist on Ni surface at high temperatures [67]. Molecular adsorption of H_2O on Ni only occurs at temperatures below 250 K [67], whereas adsorption of H_2O can occur via molecular adsorption on Pt and Au at the elevated temperatures [68]. At low temperatures below 260 K, adsorbed OH was found as water dissociation product, preferably on Ni (111) surface pre-covered with chemisorbed oxygen [69]. Based on the temperature-programmed desorption studies, it was found that the OH groups recombine between 180 and 240 K to form H_2O and O [70]. It was also shown that the OH groups adsorbed on Ni(110) surface at low temperatures recombine and desorb as H_2O at 320 K upon heating [71]. Therefore, H_2O–Ni interaction at high temperatures can be expressed as;

$$H_2O(g) \rightarrow O(Ni) + H_2(g) \quad (6)$$

Then, atomic oxygen is reduced by accepting two electrons from Ni and incorporated into YSZ by crossing Ni–YSZ boundaries. Therefore, the charge transfer reaction for H_2O dissociation through H_2O adsorption on Ni could be expressed as;

$$O(Ni) + e^-(Ni) \rightarrow O^-(Ni) \quad (7)$$

$$O^-(Ni) + e^-(Ni) \rightarrow O^{2-}(YSZ) \quad (8)$$

In addition, adsorption of H_2O on YSZ could also occur with the sticking coefficient close to 1 because of the strong interaction between oxidic surface and polar water molecules [34]. On the YSZ surface, physisorbed molecular H_2O is stable only at low temperatures [38], and H_2O adsorption followed by dissociation is the dominant process at the elevated temperatures [72]. Dissociative adsorption of H_2O on YSZ leads to OH surface species as shown by temperature-programmed desorption (TPD) spectroscopy and density functional theory (DFT) [72]. Therefore, interaction between H_2O and YSZ provides additional reaction pathway for charge transfer process, and could possibly follow the reaction steps as;

$$OH(YSZ) + e^-(Ni) \rightarrow O^-(Ni) + H(Ni) \quad (9)$$

$$O^-(Ni) + e^-(Ni) \rightarrow O^{2-}(YSZ) \quad (10)$$

$$H(Ni) + H(Ni) \rightarrow H_2(g) \quad (11)$$

To summarize, the global reaction for H_2O dissociation (eq. (3)) is simply the reverse process of H_2 oxidation (eq. (2)). However, investigation into the elementary reaction steps reveals that these two processes undergo completely different charge transfer reactions at TPBs. Currently, the availability of the experimental data for the kinetics of the charge-transfer reactions is limited, and it is difficult to quantitatively define the reaction rates for individual processes. Based on the impedance data in Figs. 4 and 5, the charge transfer reaction rate for fuel cell process (eqs. (4) and (5)) is sluggish under H_2O-rich conditions compared to the electrolysis process because the high-frequency impedance was found to be rate-limiting. Another possible explanation for low charge transfer resistance in electrolysis reaction could be the contribution of YSZ to H_2O adsorption for H_2O dissociation reaction since YSZ is practically inert toward H_2 oxidation reaction [72]. In fuel cell reaction, high-frequency arc is reduced with increasing H_2 partial pressure because exchange current density is dependent not only on the kinetic parameters but also on the concentration of the reactants, and charge transfer reaction for hydrogen spillover mechanism is accelerated by increasing the concentration of the reactant [40].

The mid-frequency arc of the fuel cell reaction was smaller than that of electrolysis reaction with 3% H_2O (Fig. 4) while the reverse tendency was observed with 50% H_2O (Fig. 5), which indicates that the polarization resistance is influenced by the reactant concentration. As mentioned earlier, the mid-frequency arc could be associated with the gas–solid interaction or surface diffusion of the adsorbed species, which is sensitive to the reactant concentration. Based on earlier discussion on the reaction mechanisms, the major surface species for fuel cell reaction is H on Ni, while that for electrolysis reaction should be O on Ni and OH on YSZ. Surface diffusion coefficient of H on Ni was reported to be 9.2×10^{-4}–1.2×10^{-3} $cm^2\ s^{-1}$ at 973 K [41,60,61] while that of O on Ni is 6.6×10^{-6}–8×10^{-5} $cm^2\ s^{-1}$ and that of OH on YSZ is 1.5×10^{-5} $cm^2\ s^{-1}$ at 973 K [34,73]. Therefore, surface transport of H on Ni is expected to be substantially faster than those of O on Ni and OH on YSZ, and the fact that the mid-frequency arcs for both fuel cell and electrolysis reactions are in the same order of magnitude in wide range of operating conditions exclude the probability that it is associated with the surface diffusion. Consequently, the mid-frequency arc could be attributed to the gas–solid interaction, and further study is needed for specific designation of the elementary process.

The low-frequency arc below 10^2 Hz was observed only in fuel cell reaction with 50% H_2O in Fig. 5. Such low-frequency process is generally attributed to gas diffusion [39] or gas conversion [74]. Gas conversion impedance is caused by the variation of the Nernst potential due to the passage of current, and usually observed in setups with a reference electrode outside the working chamber [74]. In this work, gas conversion impedance is not expected because all the measurements were performed in a single-atmosphere setup where the working and reference electrodes are placed in the same environment. Therefore, the most probable explanation for the low-frequency arc should be gas diffusion due to transport limitation. Understanding the gas diffusion impedance requires extensive study on the gas transport properties, electrode microstructure and electrochemical characteristics, and is beyond the scope of this paper. Detailed study on the gas transport through the porous electrode in fuel cell and electrolysis operations will be reported in our forthcoming paper.

The Nyquist and Bode plots in electrolysis operation under various H_2O contents are illustrated in Fig. 6(a) and (b), respectively. Fig. 6(c) shows the total polarization resistance as a function of H_2O content. It clearly shows that the polarization resistance is remarkably reduced by increasing H_2O content from 3% to 35%, and further reduction is observed with increasing H_2O content up to 50%. The minimum impedance occurs at 50% H_2O, and the polarization resistance increases with further increase of H_2O content to 60%. As seen in Fig. 6(b), the high- and low-frequency arcs were negligible in the entire operating conditions, and the major change of impedance was observed on the mid-frequency arc, which suggests that the reduction of impedance up to 50% H_2O is mainly due to increase of the reactant concentration. Increase of the impedance with further increase of H_2O content up to 60% could possibly be attributed to local oxidation of Ni. Oxidation of Ni at high pO_2 in H_2–H_2O environment was observed by Raman spectroscopy [75], transmission X-ray microscopy (TXM) [76,77], and X-ray absorption near edge structure (XANES) spectroscopy [78]. Oxidation of Ni is undesirable in the electrochemical aspect because existence of NiO in Ni–YSZ electrode leads to performance degradation due to loss of catalytic activity and electronic conductivity [43], and Ni–NiO transformation is also accompanied by large volume change which can cause internal stress and crack formation [79]. Therefore, the

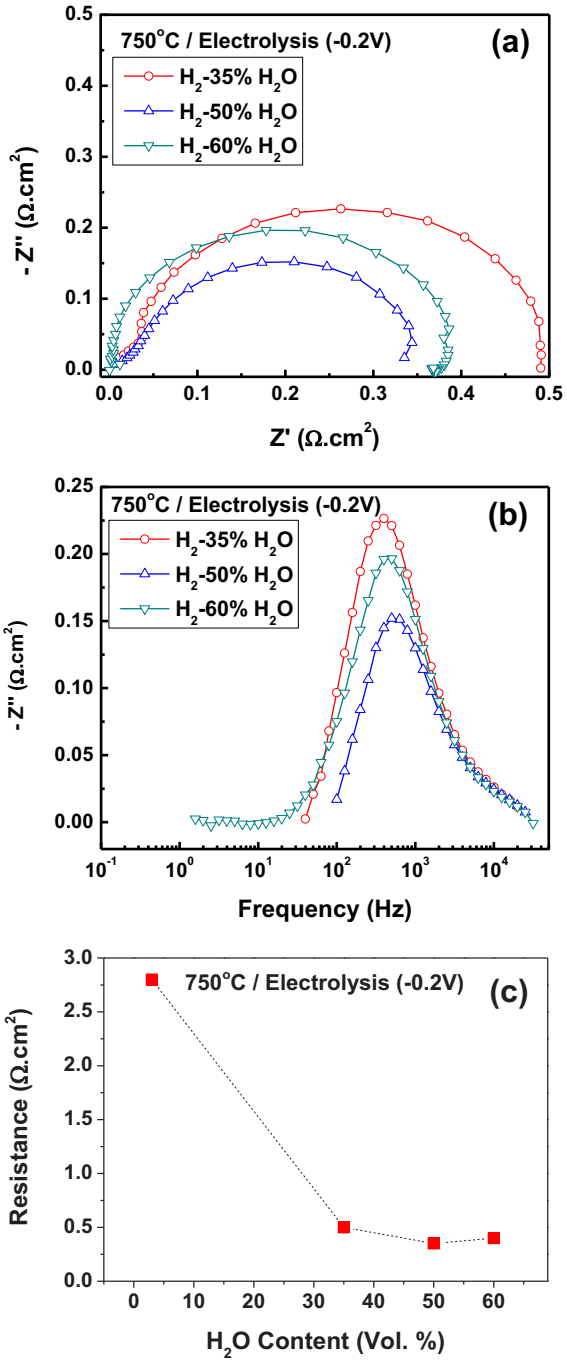

Fig. 6. (a) Nyquist and (b) Bode plots of the impedance spectra measured in electrolysis mode (−0.2 V) at 750 °C with various H_2O contents (3–60%), and (c) polarization resistance as a function of H_2O content.

operating condition of Ni–YSZ electrode for high temperature electrolysis should be carefully optimized to provide sufficient amount of H_2O for sustaining the electrolysis operation while avoiding local oxidation of Ni which can cause performance degradation, and in this research, optimum gas composition was found to be 50% H_2O in H_2.

4. Conclusions

In this research, the performance of Ni–YSZ electrode, which is commonly used as the anode for SOFCs, are evaluated for hydrogen production in SOECs. In the electrolysis mode, the impedance spectra are dominated by the mid-frequency arc, which could be assigned to the gas–solid interaction, and the high-frequency arc, which is considered to be associated with the charge transfer reaction at the Ni–YSZ interface, is negligible. On the contrary, considerable contribution of high-frequency arc is observed with reduced amount of H_2 in fuel cell mode. The difference in impedance spectra for fuel cell and electrolysis modes is explained through clarification of reaction pathways for two reactions. It is found that the maximum performance for electrolysis can be obtained by the optimization of the gas environments, and the knowledge obtained from this research can be used for design of novel electrode materials and microstructures for SOECs.

Acknowledgments

This research was financially supported by the institutional research program of the Korea Institute of Science and Technology (2E22802) and the Fundamental Research and Development Program for Core Technology of Materials funded by the Ministry of Knowledge Economy, Republic of Korea. One of the authors, D.H.P., acknowledges Korea Institute of Science and Technology for the award of a STAR Post-Doc Fellowship.

References

[1] W. Dönitz, E. Erdle, International Journal of Hydrogen Energy 10 (1985) 291–295.
[2] S. Dutta, International Journal of Hydrogen Energy 15 (1990) 379–386.
[3] M.A. Laguna-Bercero, Journal of Power Sources 203 (2012) 4–16.
[4] S.N. Rashkeev, M.V. Glazoff, Applied Physics Letters 99 (2011) 173506-1–173506-3.
[5] C.M. Stoots, J.E. O'Brien, K.G. Condie, J.J. Hartvigsen, International Journal of Hydrogen Energy 35 (2010) 4861–4870.
[6] A.V. Virkar, International Journal of Hydrogen Energy 35 (2010) 9527–9543.
[7] J. Kim, H.-I. Ji, H.P. Dasari, D. Shin, H. Song, J.-H. Lee, B.-K. Kim, H.-J. Je, H.-W. Lee, K.J. Yoon, International Journal of Hydrogen Energy 38 (2013) 1225–1235.
[8] O.A. Marina, L.R. Pederson, M.C. Williams, G.W. Coffey, K.D. Meinhardt, C.D. Nguyen, E.C. Thomsen, Journal of the Electrochemical Society 154 (2007) B452–B459.
[9] G. Tsekouras, D. Neagu, J.T.S. Irvine, Energy & Environmental Science 6 (2013) 256–266.
[10] M. Keane, M.K. Mahapatra, A. Verma, P. Singh, International Journal of Hydrogen Energy 37 (2012) 16776–16785.
[11] G.B. Jung, J.Y. Chen, C.Y. Lin, S.Y. Sun, International Journal of Hydrogen Energy 37 (2012) 15801–15807.
[12] B. Yu, W.Q. Zhang, J.M. Xu, L. Chen, X. Luo, K. Stephan, International Journal of Hydrogen Energy 37 (2012) 12074–12080.
[13] Y. Chen, J. Bunch, C. Jin, C.H. Yang, F.L. Chen, Journal of Power Sources 204 (2012) 40–45.
[14] H. Khedim, H. Nonnet, F.O. Méar, Journal of Power Sources 216 (2012) 227–236.
[15] P.J. Howard, I. Szkoda, Journal of Fuel Cell Science and Technology 9 (2012) 041009.
[16] H. Nonnet, H. Khedim, F. Méar, Ionics 18 (2012) 441–447.
[17] L. Holzer, B. Iwanschitz, T. Hocker, B. Münch, M. Prestat, D. Wiedenmann, U. Vogt, P. Holtappels, J. Sfeir, A. Mai, T. Graule, Journal of Power Sources 196 (2011) 1279–1294.
[18] J. Sehested, Catalysis Today 111 (2006) 103–110.
[19] J. Sehested, J.A.P. Gelten, I.N. Remediakis, H. Bengaard, J.K. Nørskov, Journal of Catalysis 223 (2004) 432–443.
[20] A. Hauch, S.H. Jensen, J.B. Bilde-Sørensen, M. Mogensen, Journal of the Electrochemical Society 154 (2007) A619–A626.
[21] A. Hauch, S.D. Ebbesen, S.H. Jensen, M. Mogensen, Journal of the Electrochemical Society 155 (2008) B1184–B1193.
[22] G.J. Offer, P. Shearing, J.I. Golbert, D.J.L. Brett, A. Atkinson, N.P. Brandon, Electrochimica Acta 53 (2008) 7614–7621.
[23] A. Barbucci, R. Bozzo, G. Cerisola, P. Costamagna, Electrochimica Acta 47 (2002) 2183–2188.
[24] G. Hsieh, T.O. Mason, E.J. Garboczi, L.R. Pederson, Solid State Ionics 96 (1997) 153–172.
[25] A.C. Co, S.J. Xia, V.I. Birss, Journal of the Electrochemical Society 152 (2005) A570–A576.
[26] J. Winkler, P.V. Hendriksen, N. Bonanos, M. Mogensen, Journal of the Electrochemical Society 145 (1998) 1184–1192.
[27] M. Juhl, S. Primdahl, C. Manon, M. Mogensen, Journal of Power Sources 61 (1996) 173–181.
[28] M.J. Jørgensen, M. Mogensen, Journal of the Electrochemical Society 148 (2001) A433–A442.

[29] A. Atkinson, S.A. Baron, N.P. Brandon, Journal of the Electrochemical Society 151 (2004) E186–E193.
[30] S.H. Chan, X.J. Chen, K.A. Khor, Journal of Applied Electrochemistry 31 (2001) 1163–1170.
[31] J.E. Bauerle, Journal of Physics and Chemistry of Solids 30 (1969) 2657–2670.
[32] R. Barfod, M. Mogensen, T. Klemensø, A. Hagen, Y.-L. Liu, P. Vang Hendriksen, Journal of the Electrochemical Society 154 (2007) B371–B378.
[33] S. Primdahl, M. Mogensen, Journal of the Electrochemical Society 144 (1997) 3409–3419.
[34] M. Vogler, A. Bieberle-Hütter, L. Gauckler, J. Warnatz, W.G. Bessler, Journal of the Electrochemical Society 156 (2009) B663–B672.
[35] P. Holtappels, I.C. Vinke, L.G.J. de Haart, U. Stimming, Journal of the Electrochemical Society 146 (1999) 2976–2982.
[36] S.P. Jiang, S.P.S. Badwal, Journal of the Electrochemical Society 144 (1997) 3777–3784.
[37] P. Holtappels, L.G.J. de Haart, U. Stimming, Journal of the Electrochemical Society 146 (1999) 1620–1625.
[38] S. Raz, K. Sasaki, J. Maier, I. Riess, Solid State Ionics 143 (2001) 181–204.
[39] S. Primdahl, M. Mogensen, Journal of the Electrochemical Society 146 (1999) 2827–2833.
[40] W.G. Bessler, J. Warnatz, D.G. Goodwin, Solid State Ionics 177 (2007) 3371–3383.
[41] B. Bhatia, D.S. Sholl, The Journal of Chemical Physics 122 (2005) 204707–204708.
[42] Y.R. Dar, P. Vijay, M.O. Tadé, R. Datta, Journal of Electroanalytical Chemistry 677–680 (2012) 15–23.
[43] K. Eguchi, Y. Kunisa, K. Adachi, M. Kayano, K. Sekizawa, H. Arai, Chemistry Letters 24 (1995) 963–964.
[44] S. Gewies, W.G. Bessler, V. Sonn, E. Ivers-Tiffee, ECS Transactions 7 (2007) 1573–1582.
[45] S.P. Jiang, S.P.S. Badwal, Solid State Ionics 123 (1999) 209–224.
[46] J. Mizusaki, H. Tagawa, T. Saito, T. Yamamura, K. Kamitani, K. Hirano, S. Ehara, T. Takagi, T. Hikita, M. Ippommatsu, S. Nakagawa, K. Hashimoto, Solid State Ionics 70–71 (Part 1) (1994) 52–58.
[47] T. Kawada, N. Sakai, H. Yokokawa, M. Dokiya, M. Mori, T. Iwata, Journal of the Electrochemical Society 137 (1990) 3042–3047.
[48] J.F. McCann, S.P.S. Badwal, Journal of the Electrochemical Society 129 (1982) 551–559.
[49] N.L. Robertson, J.N. Michaels, Journal of the Electrochemical Society 138 (1991) 1494–1499.
[50] R.D. Armstrong, B.R. Horrocks, Solid State Ionics 94 (1997) 181–187.
[51] V.N. Chebotin, I.D. Remez, L.M. Solovieva, S.V. Karpachev, Electrochimica Acta 29 (1984) 1380–1388.
[52] C. Jin, C. Yang, F. Chen, Journal of the Electrochemical Society 158 (2011) B1217–B1223.
[53] M.V. Rao, J. Fleig, M. Zinkevich, F. Aldinger, Solid State Ionics 181 (2010) 1170–1177.
[54] D. Presvytes, C.G. Vayenas, Ionics 13 (2007) 9–18.
[55] A.J. Robell, E.V. Ballou, M. Boudart, The Journal of Physical Chemistry 68 (1964) 2748–2753.
[56] T. Setoguchi, K. Okamoto, K. Eguchi, H. Arai, Journal of the Electrochemical Society 139 (1992) 2875–2880.
[57] D.A. Dowden, I.H.B. Haining, J.D.N. Irving, D.A. Whan, Journal of the Chemical Society, Chemical Communications 0 (1977) 631–632.
[58] H. Zhu, A. Kromp, A. Leonide, E. Ivers-Tiffée, O. Deutschmann, R.J. Kee, Journal of the Electrochemical Society 159 (2012) F255–F266.
[59] K. Christmann, Surface Science Reports 9 (1988) 1–163.
[60] G.X. Cao, E. Nabighian, X.D. Zhu, Physical Review Letters 79 (1997) 3696–3699.
[61] J. Rossmeisl, W.G. Bessler, Solid State Ionics 178 (2008) 1694–1700.
[62] D. Martin, D. Duprez, The Journal of Physical Chemistry 100 (1996) 9429–9438.
[63] A. Galdikas, C. Descorme, D. Duprez, Solid State Ionics 166 (2004) 147–155.
[64] E. Wahlström, E.K. Vestergaard, R. Schaub, A. Rønnau, M. Vestergaard, E. Lægsgaard, I. Stensgaard, F. Besenbacher, Science 303 (2004) 511–513.
[65] B. Luerßen, S. Günther, H. Marbach, M. Kiskinova, J. Janek, R. Imbihl, Chemical Physics Letters 316 (2000) 331–335.
[66] L. Bultel, C. Roux, E. Siebert, P. Vernoux, F. Gaillard, Solid State Ionics 166 (2004) 183–189.
[67] C. Benndorf, C. Nobl, M. Rusenberg, F. Thieme, Applied Surface Science 11-2 (1982) 803–811.
[68] P.A. Thiel, T.E. Madey, Surface Science Reports 7 (1987) 211–385.
[69] M. Schulze, R. Reißner, K. Bolwin, W. Kuch, Fresenius Journal of Analytical Chemistry 353 (1995) 661–665.
[70] J. Shan, A.W. Kleyn, L.B.F. Juurlink, ChemPhysChem 10 (2009) 270–275.
[71] C. Benndorf, C. Nöbl, M. Rüsenberg, F. Thieme, Surface Science Letters 111 (1981) A382.
[72] A. Gorski, V. Yurkiv, D. Starukhin, H.-R. Volpp, Journal of Power Sources 196 (2011) 7188–7194.
[73] D.G. Goodwin, H. Zhu, A.M. Colclasure, R.J. Kee, Journal of the Electrochemical Society 156 (2009) B1004–B1021.
[74] S. Primdahl, M. Mogensen, Journal of the Electrochemical Society 145 (1998) 2431–2438.
[75] J.D. Kirtley, D.M. Halat, M.D. McIntyre, B.C. Eigenbrodt, R.A. Walker, Analytical Chemistry 84 (2012) 9745–9753.
[76] P.R. Shearing, R.S. Bradley, J. Gelb, F. Tariq, P.J. Withers, N.P. Brandon, Solid State Ionics 216 (2012) 69–72.
[77] G.J. Nelson, W.M. Harris, J.J.R. Izzo, K.N. Grew, W.K.S. Chiu, Y.S. Chu, J. Yi, J.C. Andrews, Y. Liu, P. Pianetta, Applied Physics Letters 98 (2011), 173109–173103.
[78] Y.-c.K. Chen-Wiegart, W.M. Harris, J.J. Lombardo, W.K.S. Chiu, J. Wang, Applied Physics Letters 101 (2012) 253901–253904.
[79] K.J. Yoon, C.A. Coyle, O.A. Marina, Electrochemistry Communications 13 (2011) 1400–1403.